AGU PUBLICATIONS

JGR

Journal of Geophysical Research: Solid Earth

RESEARCH ARTICLE

10.1002/2016JB013405

Special Section:

Slow Slip Phenomena and Plate Boundary Processes

Key Points:

- Apparent corner frequency measurements yield bounds on path-averaged *Q*
- Bulk crustal attenuation is not responsible for anomalous spectra of LFEs
- High *P*-to-*S* corner frequency ratios of LFEs may signal severe, localized near-source attenuation

Supporting Information:

- Supporting Information S1
- Table S1

Correspondence to:

M. G. Bostock,

bostock@eos.ubc.ca

Citation:

Bostock, M. G., A. M. Thomas, A. M. Rubin, and N. I. Christensen (2017), On corner frequencies, attenuation, and low-frequency earthquakes, *J. Geophys. Res. Solid Earth*, *122*, doi:10.1002/2016JB013405.

Received 26 JUL 2016

Accepted 8 JAN 2017

Accepted article online 11 JAN 2017

On corner frequencies, attenuation, and low-frequency earthquakes

M. G. Bostock[1], **A. M. Thomas**[2], **A. M. Rubin**[3], **and N. I. Christensen**[1]

[1]Department of Earth, Ocean and Atmospheric, University of British Columbia, Vancouver, British Columbia, Canada, [2]Department of Earth Sciences, University of Oregon, Eugene, Oregon, USA, [3]Department of Geosciences, Princeton University, Princeton, New Jersey, USA

Abstract We have recently suggested that the nearly constant duration of low-frequency earthquakes (LFEs) (and, equivalently, the band limitation of tectonic tremor) manifests a moment-duration scaling that is fundamentally different from regular earthquakes and is most easily explained as rupture on asperities of roughly constant dimension. In that work, we employed qualitative arguments against potential bias by attenuation. Here we examine the role of attenuation more quantitatively through an analysis that avoids specification of particular source (e.g., Brune) models and relies on the particle velocity spectral maximum as the definition of apparent corner frequency. The analysis leads to the formal definition of a saturation frequency as the limiting value of apparent corner frequency as the true corner frequency tends infinity. The saturation frequency, a formal equivalent to f_{max}, can be used to set bounds on path-averaged quality factor *Q*. We apply these relations to deep crustal and intraslab earthquakes beneath Vancouver Island to estimate bulk crustal attenuation parameters that are subsequently used to correct apparent corner frequency measurements of LFEs reported in our earlier work. The attenuation bias due to bulk crustal structure is shown to be small, with negligible effect on the principal conclusions of that study. However, a review of laboratory and seismic refraction measurements of attenuation in oceanic basalts and evidence for high *P*-to-*S* LFE corner frequency ratios raises the possibility that strong, highly localized, near-source attenuation accompanying high pore-fluid pressures could cause the bandlimited nature of LFEs through the depletion of high frequencies.

1. Introduction

Low-frequency earthquakes (LFEs) are small magnitude repeating earthquakes that occur in association with slow, aseismic slip. LFEs are peculiar in that they typically manifest in the 1–10 Hz frequency band and are depleted in high-frequency content relative to traditional earthquakes of the same moment. In a recent study [*Bostock et al.*, 2015], we examined the moment (M_0) versus duration (τ) scaling of LFEs below southern Vancouver Island, using almost 270,000 detections recorded between 2003 and 2013. Our analysis suggests that LFEs obey a scaling close to $\tau \propto M_0^{1/10}$ that is distinct from regular earthquakes, which, for the most part, conform with the expectation of self-similarity, namely, $\tau \propto M_0^{1/3}$ [e.g., *Ide and Beroza*, 2001; *Prieto et al.*, 2004]. Our result is also distinct from the $\tau \propto M_0$ scaling proposed by *Ide et al.* [2007] for general slow-slip phenomena. The simplest interpretation of the $\tau \propto M_0^{1/10}$ scaling is that LFEs occur on spatially restricted asperities such that their moment is governed primarily by slip whereas area, rupture velocity, and duration remain approximately constant. Similar interpretations have been advanced for some populations of regular earthquakes [e.g., *Harrington and Brodsky*, 2009]. Our treatment of LFEs accounted for the effects of bulk path attenuation on waveform amplitudes by incorporating attenuation factors based on tremor studies of *Baltay and Beroza* [2013] and *Yabe et al.* [2014], but not for pulse broadening through the preferential depletion of high-frequency energy. We argued that for the low frequencies that characterize LFEs, such effects would be small.

Our focus in the present work is to quantify the bias introduced by attenuation on the previously proposed LFE moment-duration scaling, by estimating bulk crustal quality factor *Q* below southern Vancouver Island using near-epicentral recordings of deep crustal and intraslab earthquakes that lie in close proximity to LFEs. Our estimation approach is somewhat unconventional in that it relies on measurements of a modeled parameter that we refer to as "saturation" frequency, which, with certain caveats, corresponds to the parameter $f_{\max}$ defined by *Hanks* [1982]. It can also be related to the κ parameter originally defined by *Anderson and Hough* [1984] that finds wide use in engineering applications [e.g., *Ktenidou et al.*, 2014]. Our derivation of saturation frequency is free of source model parameterizations [e.g., *Brune*, 1970; *Boatwright*, 1978], admits frequency-dependent attenuation, and relies on a definition of apparent corner frequency as the maximum of the particle velocity spectrum of an isolated *P* or *S* waveform. If saturation frequency can be confidently measured from small events, it may be used to estimate path-averaged *Q*. We employ this approach to estimate attenuation beneath southern Vancouver Island from recordings of small intraslab and deep crustal events. The same formulation is then used in reverse to correct the LFE apparent frequencies and proposed moment-duration scaling for bias due to attenuation.

After presenting the analytical framework of our approach in the following section, we describe the data, practical measurement of saturation frequency, and recovery of *Q* from Vancouver Island seismograms. We then correct LFE moment-duration scaling for attenuation considering both frequency-dependent and frequency-independent *Q* models. Finally, we review laboratory and seismic refraction evidence for high attenuation levels within fluid-saturated basalt that, together with suggestive evidence for unusually high *P*-to-*S* apparent corner frequency ratios for LFEs, may provide an alterative explanation for the peculiar band limitation of tremor.

2. Corner Frequencies and Attenuation From the Velocity Spectrum

We introduce a generic earthquake source model by writing the particle displacement spectrum $|u(\omega)|$ of an individual body wave phase in the absence of attenuation in the functional form:

$$|u(\omega)| = S\left(\frac{\omega}{\omega_c}\right). \tag{1}$$

The functional dependence upon ω/ω_c establishes a scaling dependent upon corner frequency ω_c. We further impose the physical constraint [*Aki and Richards*, 2002] that $S\left(\frac{\omega}{\omega_c}\right)$ tend to a constant proportional to earthquake moment M_0 at low frequencies such that

$$\lim_{\omega\to 0} S\left(\frac{\omega}{\omega_c}\right) = \text{constant} \times M_0, \qquad \lim_{\omega\to 0} \frac{\partial S}{\partial \omega} = 0. \tag{2}$$

The corner frequency ω_c will be defined here as the global maximum of the corresponding particle velocity spectrum $|v(\omega)|$:

$$|v(\omega)| = \omega\, S\left(\frac{\omega}{\omega_c}\right), \tag{3}$$

which increases over the interval $0 < \omega < \omega_c$ owing to (2) and decreases for $\omega > \omega_c$ at some rate that need not be specified for our purposes. Consequently, ω_c must satisfy

$$S(1) = -\omega_c \left.\frac{\partial S}{\partial \omega}\right|_{\omega=\omega_c}. \tag{4}$$

The family of earthquake spectral models proposed by [*Boatwright*, 1978] belongs to the class of $S\left(\frac{\omega}{\omega_c}\right)$ and was originally written as follows:

$$|u(\omega)| = \frac{M_0}{\left[1 + (\omega/\omega_b)^{n\gamma}\right]^{1/\gamma}}. \tag{5}$$

The exponents n and γ parameterize this family, and we note that the *Brune* [1970] source model is a particular case specified through $n = 2$, $\gamma = 1$ (see Figure 1). Although ω_b is nominally referred to as “corner frequency” in this representation, $|v(\omega_b)|$ does not generally correspond to the maximum of $|v(\omega)| (= |v(\omega_c)|)$. It is straightforward to show that

$$\omega_b = (n-1)^{\frac{1}{n\gamma}}\, \omega_c, \tag{6}$$

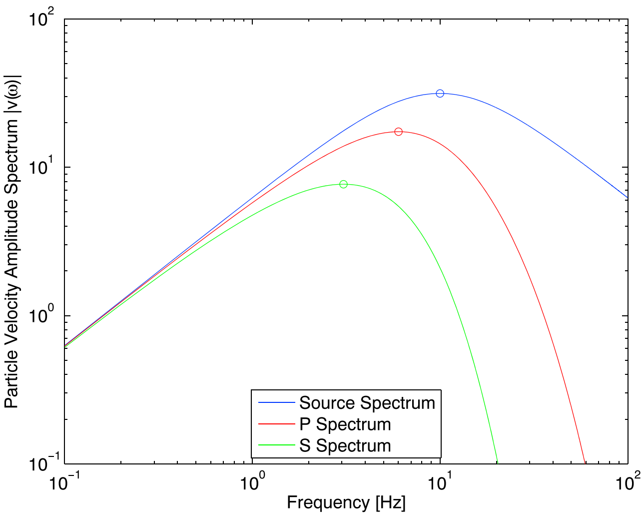

Figure 1. True source particle velocity spectrum (blue) for Brune model with corner frequency 10 Hz, and resulting *P* (red) and *S* wave (green) spectra for a model incorporating attenuation at $X = 50$ km, $Q_P = 300$, $Q_S = 150$, $V_P = 6.7$ km/s, and $V_S = V_P/\sqrt{3}$. Circles at spectral maxima are solutions to (10).

where it becomes apparent that $\omega_b = \omega_c$ only when $n = 2$. Equation (5) can thus be recast as follows:

$$|u(\omega)| = S\left(\frac{\omega}{\omega_c}\right) = \frac{M_0}{\left[1+\frac{1}{n-1}\left(\frac{\omega}{\omega_c}\right)^{n\gamma}\right]^{1/\gamma}}. \tag{7}$$

In keeping with our focus on the spectral properties of an individual *P* or *S* waveform, we model attenuation in the ray approximation through a possibly frequency-dependent t^* operator:

$$t^*(\omega) = \int_{\text{ray}} \frac{\mathrm{d}x}{V(x)\,Q(x,\omega)} = \frac{X}{\overline{V}\,\overline{Q}(\omega)}, \tag{8}$$

where $V(x)$, $Q(x,\omega)$ and $\overline{V}$, $\overline{Q}(\omega)$ are the local and path-averaged velocities and quality factors, respectively, and X is the total path length. The particle velocity spectrum in the presence of attenuation thus becomes

$$|v(\omega)| = \omega\, S\left(\frac{\omega}{\omega_c}\right)\, \mathrm{e}^{-\omega t^*(\omega)/2}. \tag{9}$$

The value of ω at which (9) is maximized now depends on both attenuation and the true source corner frequency (e.g., Figure 1) and so is termed the *apparent* corner frequency $\omega'_c = \omega'_c(\overline{Q}, \omega_c)$. It satisfies

$$S\left(\frac{\omega'_c}{\omega_c}\right)\left[\left(\omega'_c\right)^2 \left.\frac{\partial t^*}{\partial \omega}\right|_{\omega=\omega'_c} + \omega'_c t^* - 2\right] = 2\,\omega'_c \left.\frac{\partial S}{\partial \omega}\right|_{\omega=\omega'_c}. \tag{10}$$

For a given path length X, the behavior of $\omega'_c = \omega'_c(\overline{Q}, \omega_c)$ as ω_c tends to infinity leads to the definition of a saturation frequency $\hat{\omega}'_c$:

$$\hat{\omega}'_c(\overline{Q}) = \lim_{\omega_c \to \infty} \omega'_c(\overline{Q}, \omega_c), \tag{11}$$

which can be recovered from (2) and (10) and noting that

$$\lim_{\omega_c \to \infty} S\left(\frac{\omega}{\omega_c}\right) = \lim_{\omega \to 0} S\left(\frac{\omega}{\omega_c}\right), \qquad \lim_{\omega_c \to \infty} \frac{\partial S}{\partial \omega} = \lim_{\omega \to 0} \frac{\partial S}{\partial \omega}. \tag{12}$$

Accordingly, the saturation frequency must satisfy

$$\left[\left(\hat{\omega}'_c\right)^2 \left.\frac{\partial t^*}{\partial \omega}\right|_{\omega=\hat{\omega}'_c} + \hat{\omega}'_c t^* - 2\right] = 0, \tag{13}$$

which is independent of the details of the source model $S\left(\frac{\omega}{\omega_c}\right)$ beyond the physical constraints in (2).

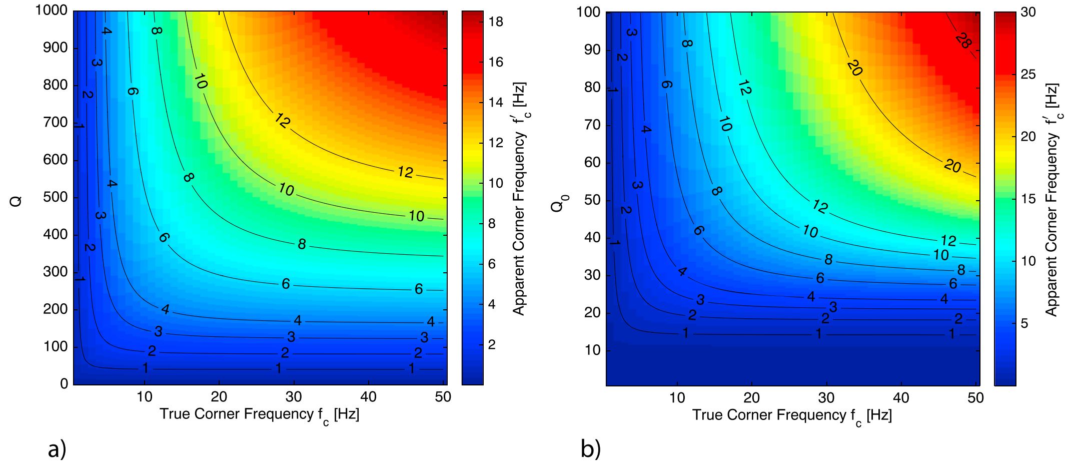

Figure 2. Apparent corner frequency f'_c as a function of true corner frequency f_c and (a) frequency-independent Q and (b) frequency-dependent $Q(f) = Q_0 f^{-\alpha}$ for $\alpha = 0.65$. Values are plotted for $x = 50$ km and $V_S = 3.85$ km/s.

Figure 2 displays two examples of apparent corner frequency as a function of path-averaged quality factor and true corner frequency for a path length of $X = 50$ km, where we rewrite radial frequencies as linear frequencies, (e.g., $f_c = \omega_c/(2\pi)$ and $f'_c = \omega'_c/(2\pi)$). In the first model (Figure 2a), we plot the results for the Brune source model with frequency-independent $\overline{Q}$. Contours of $f'_c(\overline{Q}, f_c)$ display a characteristic "L" shape. As $\overline{Q}$ tends to infinity (i.e., no attenuation), the apparent corner frequency is asymptotic to the true corner frequency, as expected. As true corner frequency tends to infinity, $f'_c(\overline{Q}, f_c)$ approaches the saturation frequency $\hat{f}'_c(\overline{Q})$, which, from (13), satisfies

$$\hat{f}'_c(\overline{Q}) = \frac{1}{\pi t^*} = \frac{\overline{Q}}{\pi\, t}, \tag{14}$$

where $t = X/\overline{V}$ is the ray theoretic traveltime. Moreover, for any given X, $\overline{V}$ pair, there is a minimum possible value of $\overline{Q}$ capable of generating an observed apparent corner frequency f'_c, such that

$$\overline{Q} \geq \pi f'_c\, t, \tag{15}$$

with strict equality attained for $f'_c = \hat{f}'_c$.

The expression in (14) is equivalent to that cited by *Hanks* [1982] in his consideration of attenuation as a cause for $f_{\max}$, the frequency at which observed far-field S wave acceleration spectra in California cease to be flat and diminish abruptly. Equation (14) is also comparable to a saturation frequency defined by *Anderson* [1986] and written here as $\hat{f}'_A$ that involves the "attenuation" parameter κ:

$$\hat{f}'_A = \frac{2}{\pi\, \mathrm{e}\, \kappa}. \tag{16}$$

We may draw an equivalence between κ and t^* if the spectrum from which $\hat{f}'_A$ is determined in (16) corresponds to an individual body wave phase for which the ray theoretic description (8) is accurate. Equation (16) can be derived as the intersection of horizontal asymptote with a linearization of exponential decay about the value of frequency at which power law (ω^{-2}) decay is realized, in the log displacement-log frequency domain. The difference between (14) and (16) demonstrates that saturation frequency depends on how source corner frequency is defined, with (1) velocity spectral maximum and (2) intersection of asymptotes definitions yielding similar but nonequivalent results.

The model shown in Figure 2b employs the Brune spectral model with a frequency-dependent attenuation parameterization of the form

$$\overline{Q} = Q_0\, f^{\alpha}, \qquad t^* = t^*_0\, f^{-\alpha}, \tag{17}$$

where Q_0 and $t^*_0 = X/(Q_0 \overline{V})$ are reference values at $f = 1$ Hz. The general behavior is similar to that in Figure 2a, with well-defined vertical and horizontal asymptotes, although the latter is shifted to lower values of quality factor due to the increased attenuation per wavelength at low frequencies. The saturation frequency defining the horizontal asymptote in this case can be shown to equal

$$\hat{f}'_c(Q_0) = \left[\frac{2}{\pi\, t_0^*\,(1-\alpha)}\right]^{1/(1-\alpha)} = \left[\frac{Q_0}{\pi\, t\,(1-\alpha)}\right]^{1/(1-\alpha)} . \tag{18}$$

In analogy with (15), we may place a minimum bound on Q_0 for any observed f'_c:

$$Q_0 \geq \pi\,(f'_c)^{1-\alpha}\,(1-\alpha)\,t, \tag{19}$$

with equality once more attained at $f'_c = \hat{f}'_c$. A single measurement of $\hat{f}'_c$ will thus suffice to provide an estimate of Q_0 assuming a value of α. If multiple measurements of $\hat{f}'_c$ are available for different distances X and the sampled medium is homogeneous, then α can, in principle, be determined as the value that minimizes variance across individual Q_0 estimates via a line search. In practice, spectrum curvature as employed in parametric fitting [e.g., *Stachnik et al.*, 2004] will yield better constrained estimates of α.

3. Constraints on Q Within the Cascadia Forearc

Our interest in attenuation is motivated by a desire to quantify its potential effects in biassing estimates of corner frequencies of southern Vancouver Island LFEs reported in *Bostock et al.* [2015]. In the previous section, we have shown that any observed apparent corner frequency f'_c supplies a lower bound on the path-averaged quality factor $\overline{Q}$ for a given X, $\overline{V}$ pair (equations (15) and (19)). Consequently, the highest lower bound for $\overline{Q}$ will come from seismic events with apparent corner frequencies that approach their saturation values defined in (14) for frequency-independent attenuation or, more generally, in (18). LFEs are, by their band-limited, low-frequency and low-amplitude nature, ill suited for the purpose of estimating attenuation, and so we turn to intraslab and deep (>20 km) crustal events that sample similar bulk crustal structure but are characterized by significantly higher corner frequencies. From the resulting $\overline{Q}$ estimates we may then quantify the likely bias induced in apparent corner frequency measurements f'_c of LFEs away from their true values f_c.

We employ 100 samples per second (sps) data recorded at Portable Observatories for Lithospheric Analysis and Research in Seismicity (POLARIS) stations KLNB, MGCB, SSIB, and TWKB between 2002 and 2006 [*Nicholson et al.*, 2005] (note under KLNB, we consider two sites: KELB and KLNB occupied in 2002–2003 and 2004–2006, respectively, and separated by ~100 m). These stations employed Guralp CMG3-ESP seismometers purchased concurrently with the same nominal response (flat to velocity from 0.01 to 50 Hz). They also formed part of the *Bostock et al.* [2015] study though they were resampled to 40 sps therein to facilitate analysis and comparison with data from other stations in the region. Figure 3 displays a map of station locations and the epicenters of various classes of seismic events. Table 1 provides hypocentral information on 27 events for which apparent corner frequencies f'_P, f'_S (values of f'_c specific to P and S waves, respectively), could be confidently measured from well-defined peaks in the particle velocity spectra of P and S windows chosen to represent the primary body wave signal. This selection consists primarily of events with local magnitudes $M_L \leq 1.1$ that are likely to possess true corner frequencies well above 10 Hz and also includes several of the largest ($M_L \geq 2.1$) events that occurred during the deployment period, for comparative purposes. Events 040424 and 040322 are worth noting. The former event represents the largest (M_L=2.1) member of a sequence of some 30 repeating, deep crustal events north of station PGC that occurred between March and May 2004. The sequence also includes event 040322, the smallest ($M_L \sim -0.5$ based on a maximum absolute amplitude ~450 times smaller than that of event 040424, see Figure 4), visually identified member of the sequence. Spectra were computed using multitaper estimates (from 7 Slepian tapers and a time half bandwidth product of 4), over windowed vertical components for P wave spectra, and as the mean of windowed north and east components for S wave spectra. Multitaper spectral analysis produces well-constrained, stable spectral estimates in portions of the earthquake spectrum that have large amplitude [e.g., *Park et al.*, 1987; *Prieto et al.*, 2004], as at f'_c. An example is shown in Figure 5. The events represent a selection of deep crustal (>20 km) and intraslab (>30 km) earthquakes from the Geological Survey of Canada earthquake catalogue for the POLARIS deployment period.

In Figure 6, we present several summary plots of corner frequency measurements and related quantities. Figure 6 (left column) displays plots of $\log_{10}(f'_P)$, $\log_{10}(f'_S)$ versus M_L. In the absence of attenuation, we would expect these measurements to lie along a line of slope −3, reflecting the generally recognized self-similarity of regular earthquakes. In contrast, both quantities appear largely independent of magnitude. f'_S displays considerably less variability than f'_P for stations TWKB, MGCB, and SILB, with TWKB characterized by the highest

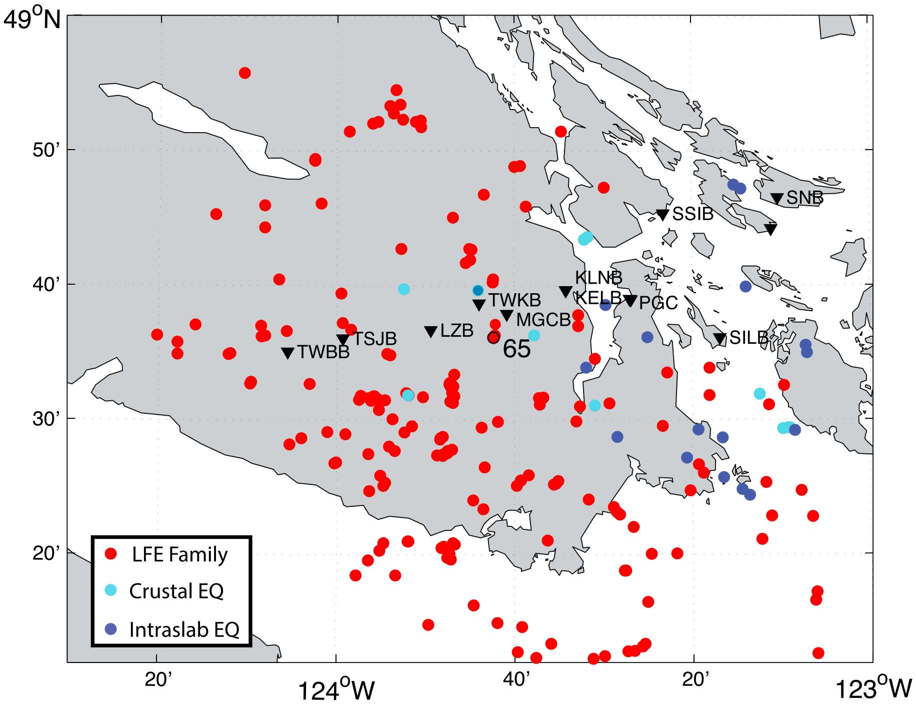

Figure 3. Map of stations (black inverted triangles), LFEs (red dots), crustal (cyan dots), and intraslab (blue dots) earthquakes considered in this study. The epicenter corresponding to template 065, referred to in Figure 8, is labeled and located immediately to the southwest of station MGCB.

values (25–35 Hz), MGCB and SILB falling dominantly between 9 and 15 Hz, and KLNB exhibiting the largest range of variation. Ranges for f'_P exhibit less obvious control by station. Recordings for the two largest events ($M_L > 3.0$) display the lowest apparent P corner frequencies (∼10 Hz) suggesting a waning influence of attenuation for higher magnitude events. This trend to lower apparent frequencies for larger magnitude events is less obvious for f'_S, for which there are examples of smaller events that also share lower apparent corner frequencies, suggesting increased attenuation due to the larger number of wavelengths per unit distance traveled. This contention is supported by Figure 4 in which P and S waveforms for repeating events 040322 and 040424 are displayed in black and red, respectively. S waveforms for the two events are very similar indicating minor differences in spectral content, whereas P waveforms display significantly lower frequency content for the larger, $M_L = 2.1$ event. This observation further suggests that apparent S corner frequency measurements f'_S closely approach their saturation values $\hat{f}'_S$ for events $M_L \leq 2.1$ and the path lengths considered [cf., *Hanks*, 1982].

Plots of f'_P, f'_S versus raypath length are shown in Figure 6 (right column). In a strongly attenuating, homogeneous medium where apparent corner frequencies approach their saturation values, we would anticipate that apparent corner frequency decrease as $1/X$ as per (14) and (18). Unsurprisingly, given the results above, there is little evidence for such a dependence; apparent corner frequencies are, as before, largely controlled by station, an effect that is more pronounced for S waves than for P waves. The collective behavior of apparent corner frequencies as functions of magnitude and raypath length, namely, that they are strongly controlled by station, most likely indicates that near-surface site effects have a dominating influence upon apparent corner frequency measurements above 10 Hz for $M_L < 1.0$, and particularly so for S waves [e.g., *Ktenidou et al.*, 2014]. We proceed to consider the data in Figures 6 and 7 and their implications for LFE spectral estimates in light of a nominal model for attenuation under the assumption that near-receiver effects are adequately described within the ray theoretic description (8).

4. Bias in LFE *S* Corner Frequencies Due To Crustal Attenuation

To examine the effect of attenuation on the estimation of LFE corner frequencies described by *Bostock et al.* [2015], we first consider a Brune spectral model where we focus on S waves and adopt a value Q_S that is

Table 1. Origin Times, Hypocenters, and Local Magnitudes of Regular Earthquakes Examined in This Study, as Determined by the Geological Survey of Canada

Date (YYMMDD)	Time (HH:MM:SS)	Latitude (°N)	Longitude (°E)	Depth (km)	M_L
020921	00:55:20	48.490	−123.151	26.2	4.3
020926	07:00:04	48.489	−123.164	24.8	2.8
021016	08:05:43	48.453	−123.344	45.0	0.8
030114	00:06:05	48.490	−123.154	25.8	2.4
030710	23:45:51	48.786	−123.241	54.1	0.8
030906	23:08:26	48.663	−123.874	23.7	0.8
030911	14:29:35	48.791	−123.254	55.4	0.6
031002	08:45:55	48.531	−123.866	22.1	0.3
031012	03:42:36	48.407	−123.227	44.8	2.4
031112	23:21:09	48.605	−123.630	21.8	0.9
040322	13:14:35	48.727	−123.529	25.3	−0.5
040424	06:00:15	48.727	−123.529	25.3	2.1
040708	02:31:16	48.583	−123.118	51.2	0.5
040906	04:52:32	48.478	−123.277	47.2	0.8
041004	18:46:14	48.487	−123.142	54.3	0.9
050104	18:53:09	48.532	−123.207	31.1	1.1
050108	07:58:38	48.661	−123.735	20.5	1.0
050417	00:44:14	48.643	−123.496	45.9	1.0
050422	12:55:40	48.603	−123.417	46.8	0.9
050506	13:00:45	48.479	−123.474	43.5	0.7
050616	12:16:30	48.592	−123.121	45.7	0.8
050618	20:31:05	48.488	−123.322	46.9	0.7
050624	02:51:00	48.665	−123.232	54.8	0.3
050625	08:36:44	48.429	−123.275	46.7	0.4
050710	08:45:59	48.518	−123.516	27.1	0.3
060115	12:29:45	48.565	−123.533	44.4	3.6
060308	04:56:03	48.414	−123.241	48.0	0.5

independent of frequency. In our choice of a nominal value $Q_S = 450$, we have considered station SILB that displays comparable minimum bounds on Q for P and S waves with medians of 454 and 482, respectively (see Figure 7). We employ a traveltime of $t = 13$ s corresponding to a median path length of 50 km and an S velocity of 3.85 km/s. Observations of apparent LFE corner frequencies by *Bostock et al.* [2015] led to their proposal of a model for moment-duration scaling, $\tau \propto M_0^{1/10}$, that differs significantly from that expected for self-similarity, namely, $\tau \propto M_0^{1/3}$ (note that duration is inversely proportional to corner frequency, $\tau \propto f_c^{-1}$). Their interpretation would imply that LFE sources are governed by an intrinsic temporal scale unlike regular earthquakes or other slow-slip phenomena that obey $\tau \propto M_0$ [*Ide et al.*, 2007]. Observed LFE moment magnitudes range between approximately M_w 1.0 and 2.5, corresponding to a ratio of moments of about 177. The range of observed apparent corner frequencies corresponds to approximately 1.5–2.5 Hz, consistent with the proposed scaling (i.e., $2.5/1.5 \approx 177^{0.1}$). We assume a Brune model and employ the analytical framework developed in previous sections for the material (Q_S, V_S) and geometric (X) properties specified above, to map the apparent corner frequency range of [1.5, 2.5] Hz to a true corner frequency range of [1.733, 3.157] Hz, a relatively minor distortion (and one which could be considered an upper bound, given the minimum-bound nature of the employed Q estimate). Moreover, the effect on scaling is also small, with the original relation revised to $\tau \propto M_0^{0.116}$. These calculations provide quantitative support for the more qualitative justifications made by *Bostock et al.* [2015] for ignoring the effects of bulk crustal attenuation on LFE corner frequency determination.

We note, however, that there is evidence from a study of attenuation within the Alaska subduction zone supporting the existence of frequency-dependent Q within a tectonic environment similar to southern Vancouver Island. *Stachnik et al.* [2004] reported that attenuation of primary body wave phases through the Alaskan

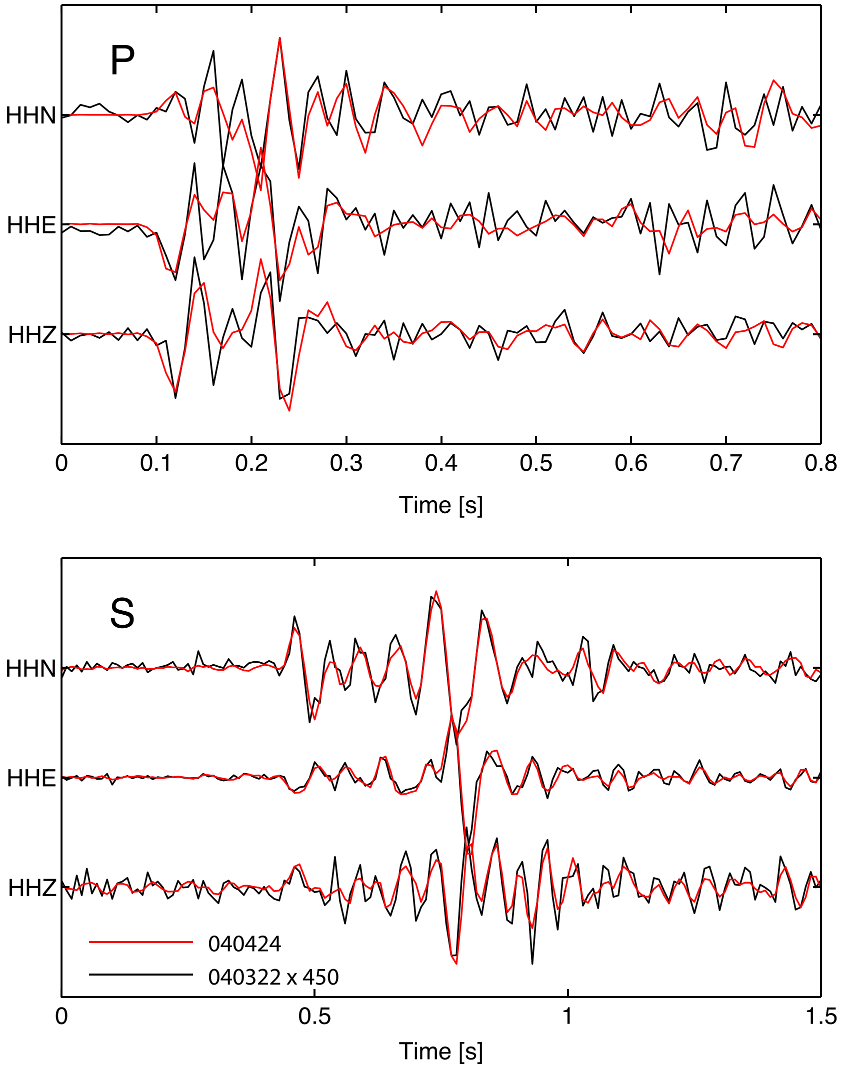

Figure 4. Amplitude-normalized (top) *P* waveforms and (bottom) *S* waveforms for repeating crustal events 040322 (black, $M_L \approx -0.5$) and 040424 (red, $M_L = 2.1$) recorded at station SSIB (see Table 1). Maximum absolute amplitude of event 040424 is 450 times that of 040322. Alignment of *P* and *S* seismograms is accomplished with a single, common time shift.

fore-arc crust and uppermost slab mantle was best modeled with a frequency dependence of the form defined in (17) with $\alpha = 0.65$, using the Brune spectrum. We adopt this representation to examine frequency dependence on LFE observations below southern Vancouver Island and employ a value of $Q_{0S} = 33.6$, determined once more as the median for data collected at SILB (Figure 7) using (19). In this case the apparent corner frequency band [1.5, 2.5] Hz is mapped to true corner frequencies of [2.579, 4.901] Hz. This distortion is larger than that for constant Q_S owing to the fact that low frequencies experience higher attenuation per wavelength than high frequencies. The revised frequency band translates to a moment-duration scaling of $\tau \propto M_0^{0.124}$ which, again, does not alter the principal conclusions drawn by *Bostock et al.* [2015].

5. LFE Corner Frequencies Ratios and High Attenuation at the LFE Source

In the preceding section, we have shown that bulk crustal attenuation is unlikely to significantly bias LFE corner frequency measurements or the LFE moment-duration scaling proposed by *Bostock et al.* [2015]. We proceed now to consider a second potential source of attenuation bias, namely, the possibility that *Q* values in the immediate vicinity of the LFE source are anomalously low. We outline supporting evidence for this conjecture in the form of high frequencies characterizing *P* waveforms for the strongest LFE detections, and attenuation measurements on fluid-saturated basalts in lab samples and in in situ seismic refraction profiles.

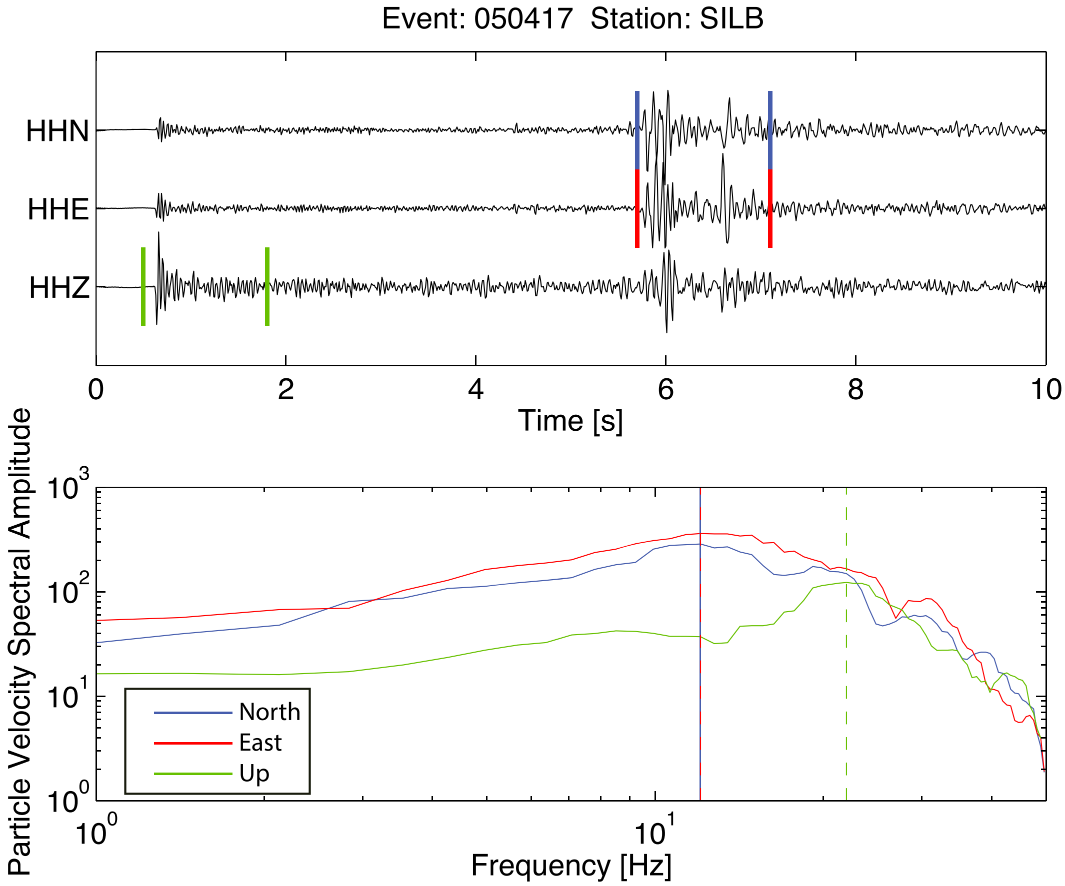

Figure 5. (top) Example waveforms and (bottom) velocity spectra (*P* wave is green; *S* waves on north and east components are blue and red, respectively) for event 050417 recorded at station SILB.

For regular earthquakes, *S* wave corner frequencies are generally recognized to be lower than those for *P* waves due to the stronger influence of directivity on the former [e.g., *Sato and Hirasawa*, 1973; *Aki and Richards*, 2002]. When averaged over the focal sphere, modeled ratios of *P* to *S* wave corner frequencies typically lie close to 1.5 [*Madariaga*, 1976]. *Bostock et al.* [2015] noted that *P* and *S* waveforms on LFE templates displayed no discernable difference in corner frequency, such that both modes were analyzed together. The assumption in that work was that directivity effects were muted possibly due to the predominance of subvertical paths from the subhorizontal plate boundary rupture surface. This geometry implies that raypaths are limited to small angles away from the fault normal where the effects of directivity are least significant, and for which *P* and *S* wave corner frequencies are anticipated to be most similar.

Individual detection *P* waveforms from LFEs are significantly more difficult to identify than *S* waveforms at small epicentral distances since the shallowly dipping thrust source leads to a near-vertical auxiliary nodal plane [*Armbruster et al.*, 2014]. However, *P* signals do appear to emerge above background noise levels for larger, isolated LFEs associated with rapid tremor reversals [*Houston et al.*, 2011; *Bostock et al.*, 2015], located in close proximity to the axis of the POLARIS array and characterized by the highest signal-to-noise ratios. Two example detections for template 065 are shown in red in Figure 8 with corresponding template waveforms plotted in black. Modal decomposition operators (see *Kennett* [1991], including a splitting correction for *S* [*Matharu et al.*, 2014]) have been determined for the template waveforms and subsequently applied to corresponding detection waveforms to produce *P* and *S* wave signals with enhanced signal-to-noise ratio. The hypocenter for this template lies at 39.8 km depth, a few kilometers to the SSW of station MGCB (see Figure 3). The *S* waveforms of higher-quality detections display dominant frequencies that are comparable to their template counterparts, suggesting *S* wave corner frequencies near 2.0 Hz. In contrast, where noise levels permit comparison, *P* signals appear to be characterized by significantly higher dominant frequencies, see, for example, stations SILB, SSIB, and PGC for the detection on 18 July 2004 and stations

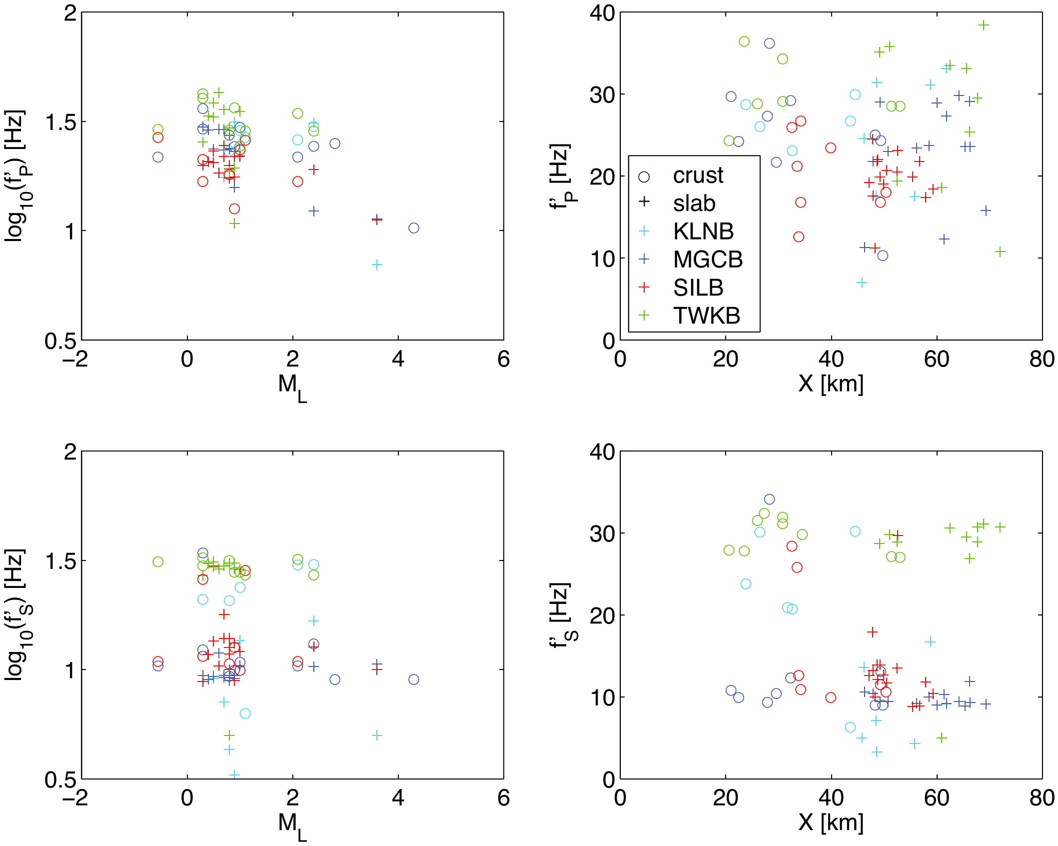

Figure 6. Plots of apparent corner frequencies f'_P, f'_S versus local magnitude M_L and raypath length X are color coded by station for deep crustal (circles) and intraslab earthquakes (crosses).

TWKB, TSJB, and TWBB on 16 September 2005 (shown in expanded scale in Figure 9). Although noise levels preclude a calculation of meaningful spectra, simple peak-to-trough durations (multiplied by 2) yield estimates of apparent *P* corner frequency between 5 and 10 Hz at these stations for these and other high signal-to-noise ratio detections. Station SNB represents an outlier with typical values near 3 Hz, possibly representing very strong near-receiver attenuation, which may help explain why the station was successful in identification of *P* wave signals by correlation with *S* waveforms in the study of *Armbruster et al.* [2014].

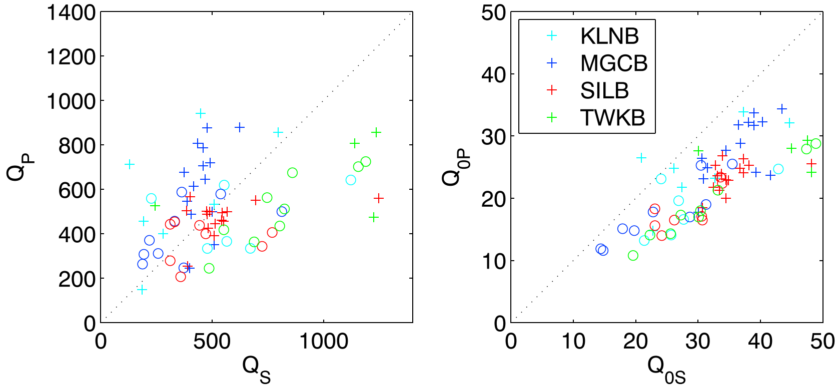

Figure 7. Plots of (left) frequency-independent Q_P versus Q_S and (right) frequency-dependent attenuation parameters Q_{0P} versus Q_{0S}. Stations are coded by color. Results from intraslab and crustal events are shown as crosses and circles, respectively.

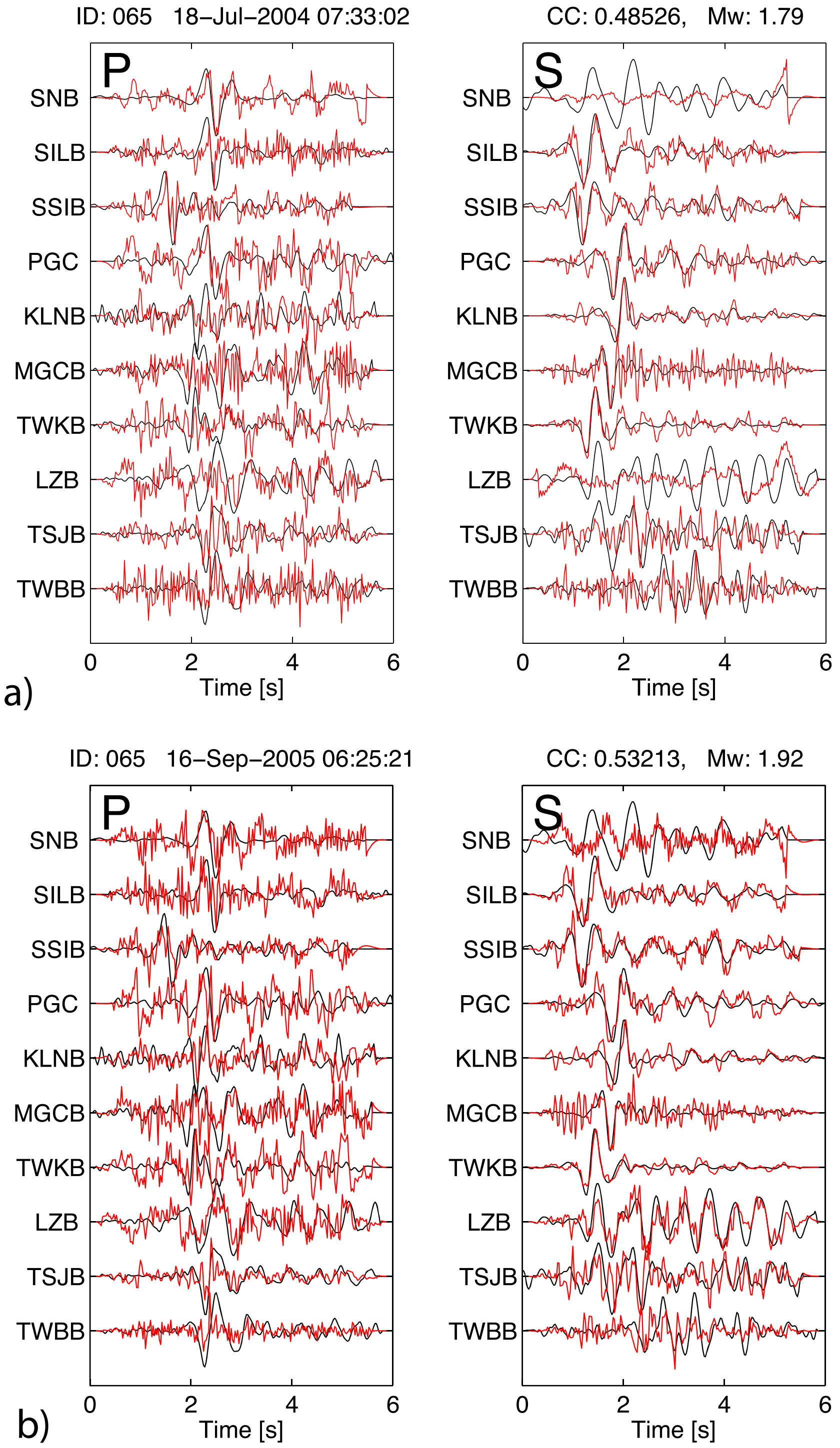

Figure 8. (a and b, left) *P* waveforms and (a and b, right) *S* waveforms for LFE templates (black) and single detections (red) on 18 July 2004 (Figure 8a) and 16 September 2005 (Figure 8b). Waveforms have been high-pass filtered (eight-pole, two-pass Butterworth) at 0.8 Hz and cosine tapered over the first and final second.

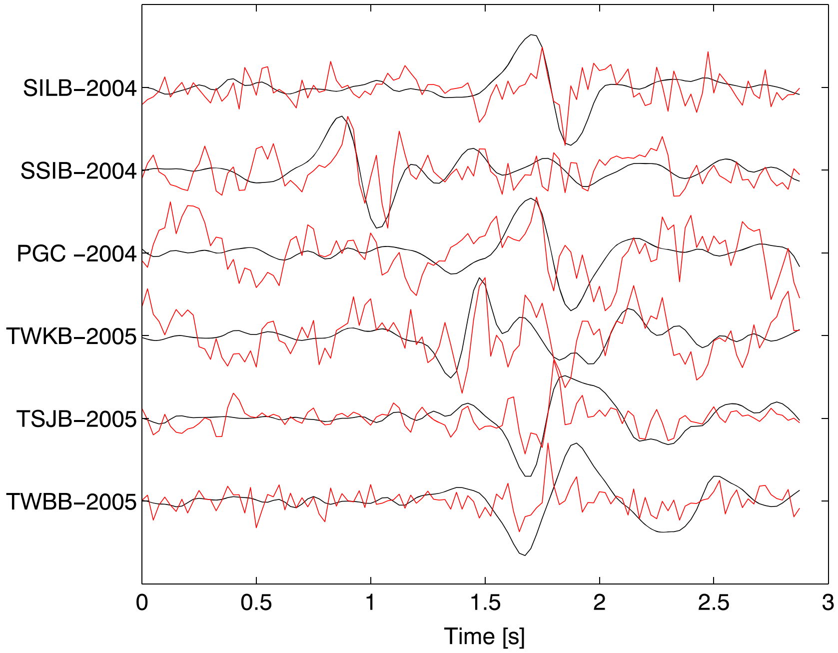

Figure 9. P waveforms at expanded scale for LFE templates (black) and single detections (red) on 18 July 2004 at stations SILB, SSIB, and PGC and on 16 September 2005 for stations TWKB, TSJB, and TWBB. Note suggestion of higher frequencies on individual detection waveforms.

We suspect that the markedly lower frequencies on template (versus detection) P waveforms results from a network-correlation-coefficient-based alignment that is controlled by higher amplitude S signals leading to misstacking of P signals from nearby but noncolocated LFEs.

Thus LFE corner frequency ratios $f_P/f_S > 2.5$ are implied and difficult to explain using simple kinematic descriptions of source directivity [*Molnar et al.*, 1973]. One possible explanation involves extreme variations in Q_P and Q_S within the LFE source region. A variety of evidence, including seismic imaging [e.g., *Shelly et al.*, 2007; *Audet et al.*, 2009], tidal modulation of tremor and LFEs [e.g., *Rubinstein et al.*, 2008; *Houston*, 2015; *Royer et al.*, 2015] and triggered tremor from passing surface waves [e.g., *Rubinstein et al.*, 2007] supports the existence of high pore-fluid pressures where LFEs and tremor occur. The seismic evidence involves observations of high (>2) V_P/V_S ratios within a thin low-velocity zone (LVZ) that coincides with LFE hypocenters. This signature is interpreted by *Hansen et al.* [2012] as due primarily to overpressured basalts of layer 2 plus or minus marine sediments, based on comparisons with laboratory measurements [*Christensen*, 1984; *Peacock et al.*, 2011] and field observations [e.g., *Salisbury and Christensen*, 1978]. Laboratory measurements of Q_S/Q_P indicate that this quantity is a decreasing function of fluid-saturated porosity, and so decreases as V_P/V_S increases. Figure 12 of *Tompkins and Christensen* [2001] presents a compilation of such data that include oceanic basalts and demonstrates this dependence at ultrasonic frequencies out to values of $V_P/V_S \approx 1.9$ and $Q_S/Q_P \approx 0.1$. Although the possibility of scale dependence in mechanisms responsible for attenuation at seismological versus ultrasonic scales must be considered, the large values of V_P/V_S (∼2.35) inferred for LFE source regions [*Audet et al.*, 2009] could thus imply small Q_S/Q_P and potentially afford an explanation for the enigmatic low-frequency signature of tremor.

For illustrative purposes, consider a simple calculation wherein we interpret the apparent corner frequency measured for S waves from LFEs to be a saturation frequency (i.e., $f'_S = \hat{f}'_S = 2.0$ Hz) caused by strong, near-source attenuation within the LVZ. Assuming frequency-independent attenuation, we may use equation (14) along with some nominal values for path lengths and physical properties to estimate Q_S of the LVZ. We consider a 50 km total path length comprising a 1 km transit through the LVZ with $V_S = 2.0$ km/s, $V_P/V_S = 2.5$ combined with 49 km traveled through bulk continental crust with $V_S = 3.85$ km/s, $V_P/V_S = \sqrt{3}$, and $Q_S = Q_P = 450$. The average $Q_S V_S$ product for the entire path is 100π km/s (see (14)), which in turn implies a value of $Q_S = 3.8$ for the LVZ using (8). If the true crustal Q_S is higher than that assumed above, the LVZ Q_S will be lower, but not significantly so since attenuation is dominated by the LVZ (a doubling of crustal Q_S to

900 yields an LVZ Q_S of 3.4). Unfortunately, we are not aware of Q_S values reported for in situ upper oceanic crust (layer 2). Laboratory values of Q_S for basalt reported by *Tompkins and Christensen* [2001] range down to 5.2, but those authors were unable to obtain adequate signal-to-noise ratios for 18 of 32 samples with the lowest Q_P values (and so likely the lowest Q_S values). Hence, they acknowledge a sampling bias and that the lowest Q_S values for their data set are likely significantly less than 5.2.

We may also compare this calculation of LVZ $Q_S = 3.8$ with reported in situ values of Q_P for layer 2 in young oceanic crust from refraction profiles compiled by *Tompkins and Christensen* [1999] (including three studies of a total of five from the Juan de Fuca ridge). These values range between 10 and 100 with a majority falling between 10 and 20. Assuming comparable values ($Q_P = 10, 20$ and hence relatively modest $Q_S/Q_P = 0.38, 0.19$) for the LVZ, we may work backward through this calculation to predict *P* wave saturation frequencies of 8.75 and 12.1 Hz, respectively. These values roughly coincide with the range of dominant *P* wave frequencies estimated from records like that in Figure 9.

These calculations, based on and/or consistent with field and laboratory measurements of rock physical properties, support the hypothesis that true LFE corner frequencies could be significantly higher than 12 Hz but are biassed to saturation values in particle velocity spectra owing to pronounced, near-source attenuation associated with high pore-fluid pressure. A similar proposition has been advanced previously by *Gomberg et al.* [2012] based on analysis of spectral decay rates for seismicity in Washington state. A corollary is that the LFE moment-duration scaling proposed by *Bostock et al.* [2015] could be invalid. There appears, however, to be one key piece of evidence that is difficult to reconcile with such an interpretation, namely, the appearance of high frequencies ($\geq$10 Hz) in *S* waves of intraslab events and the observation that high pore-fluid pressures, as revealed by $V_P/V_S \sim 2.35$, are prevalent throughout the tremor-prone fore-arc region [*Audet et al.*, 2009; *Hansen et al.*, 2012]. One would predict, given the anticipated overlap in path distribution at LVZ levels implied in Figure 3 for waves originating at LFEs and intraslab earthquakes, that signals from intraslab earthquakes would exhibit still more severe *S* wave attenuation than those from LFEs given that their raypaths traverse the LVZ in its entirety as opposed to a short transit confined to the vicinity of its upper boundary [*Nowack and Bostock*, 2013]. We note that *Yabe et al.* [2014] present evidence for path-dependent, increased attenuation in intraslab earthquakes compared to tremor, but not to the extent of significantly distorting the earthquake spectrum. *Gomberg et al.* [2012] have also suggested increased attenuation for events traveling through the LVZ region, but their analysis of events for Washington and southernmost Vancouver Island did not include any intraslab earthquakes from the latter region and so their results may be influenced by *Q* variations in bulk crustal structure, namely, pronounced low-velocity material underlying the Olympic Peninsula (see their Figure 3). The *Q* estimates for southern Vancouver Island based on saturation frequency in Figure 7 either show little evidence for significant differences between crustal and intraslab events for frequency-independent *Q* (Figure 7, left) or the suggestion of reduced frequency-dependent *Q* for crustal events (Figure 7, right). The latter trend runs counter to the expectation for a highly attenuating LVZ.

A reconciliation of the widespread, high V_P/V_S LVZ and high-frequency *S* waveforms from intraslab events with a model for LFE spectra controlled by strong near-source attenuation would appear to require (a) that the high V_P/V_S ratios that define the LVZ and imply high pore-fluid pressures need not imply low Q_S and Q_S/Q_P and (b) that low Q_S and Q_S/Q_P are not only spatially confined in a vertical sense but also laterally such that they exist only in the immediate LFE hypocentral region. If the latter condition holds, then it suggests the possibility of highly localized variability in other physical properties, most notably friction that must govern the generation of LFEs in the first place.

6. Conclusions

We have examined the effect of attenuation bias on earthquake corner frequency as measured by the particle velocity spectral maximum for a generic description of the earthquake source spectrum. This analysis leads to the definition of a saturation frequency for a given attenuation model and source-receiver path and minimum bounds on path-averaged *Q* for a given observed apparent corner frequency. These relations are applied in the analysis of a suite of deep (>20 km) crustal and intraslab earthquakes below southern Vancouver Island for which saturation frequencies appear to be reached for events $M_L \leq 1.0$. Although there is considerable variability in crustal *Q* estimates that is likely associated primarily with near-receiver attenuation, we have chosen representative, but conservative estimates of path-averaged constant and frequency-dependent *Q* to examine biassing effects on LFE corner frequencies. The bias due to bulk crustal structure is shown to be small owing to the low frequencies that dominate LFE velocity spectra (roughly equivalent to the corner frequency of an $M_w \sim 4.5$ regular earthquake). Hence, crustal attenuation is unlikely to invalidate the conclusions drawn by *Bostock et al.* [2015] concerning LFE moment-duration scaling ($\tau \sim M_0^{\frac{1}{10}}$). That scaling implies a relatively constant LFE source duration, perhaps most simply interpreted as resulting from a relatively constant asperity dimension.

We have also presented evidence that suggests apparent P wave corner frequencies of LFEs lie between 5 and 10 Hz and so differ significantly from the ~2 Hz signals observed for S waves, with a resulting ratio that is considerably higher than the average corner frequency ratio $f_P/f_S \sim 1.5$ expected for regular earthquakes. Laboratory measurements of attenuation in fluid-saturated basalts at high pore pressure indicate that anomalously low Q_S, Q_P, and Q_S/Q_P are likely to accompany high V_P/V_S characterizing the LVZ in which LFEs originate. We have shown through simple calculations that interpretation of LFE apparent S wave corner frequencies as saturation frequencies leads to estimates of LVZ Q_S consistent with available lab measurements, and that in situ seismic refraction estimates of layer 2 Q_P predict LFE P wave saturation frequencies comparable to those inferred from observations. Consequently, strong source-localized P and S wave attenuation accompanying high pore-fluid pressures could provide an explanation for the nearly constant duration of LFEs (or, equivalently, the band limitation of tremor) and invalidate the moment-duration scaling proposed by *Bostock et al.* [2015]. However, issues remain with both this explanation and the alternative that LFEs originate from asperities with approximately constant dimension. Resolution of these issues constitutes fruitful ground for future research.

Acknowledgments
Seismological data employed in this study are archived at the Geological Survey of Canada and available via the Earthquakes Canada website: http://www.earthquakescanada.nrcan.gc.ca/stndon/wf_index-en.php. Individual Q measurements and related information are provided in Table S1 in the supporting information. We are grateful to Annemarie Baltay and Heidi Houston for careful and constructive reviews that significantly improved presentation of this material. Thanks also to Yariv Hamiel and Thomas Hanks for helpful discussion and special Editor Yehuda Ben-Zion for review adjudication. This study was supported by NSERC Discovery grant RGPIN-2016-04239 to M.G.B., NSF EAR award 1520238 to A.M.T. and NSF EAR award 1344948 to A.M.R.

References

Aki, K., and P. G. Richards (2002), *Quantitative Seismology*, 2nd ed., Univ. Sci. Books, Sausalito, Calif.

Anderson, J. G. (1986), Implication of attenuation for studies of the earthquake source, in *Earthquake Source Mechanics*, vol. 37, edited by S. Das, J. Boatwright, and C. H. Scholz, pp. 310–318, AGU, Washington, D. C.

Anderson, J. G., and S. E. Hough (1984), A model for the shape of the Fourier amplitude spectrum of acceleration at high frequencies, *Bull. Seismol. Soc. Am.*, *74*, 1969–1993.

Armbruster, J. G., W.-Y. Kim, and A. M. Rubin (2014), Accurate tremor locations from coherent S and P waves, *J. Geophys. Res. Solid Earth*, *119*, 5000–5013, doi:10.1002/2014JB011133.

Audet, P., M. G. Bostock, N. I. Christensen, and S. M. Peacock (2009), Seismic evidence for overpressured subducted oceanic crust and megathrust fault sealing, *Nature*, *457*, 76–78.

Baltay, A. S., and G. C. Beroza (2013), Ground-motion prediction from tremor, *Geophys. Res. Lett.*, *40*, 6340–6345, doi:10.1002/2013GL058506.

Boatwright, J. (1978), Detailed spectral analysis of two small New York state earthquakes, *Bull. Seismol. Soc. Am.*, *68*, 1117–1131.

Bostock, M. G, A. M. Thomas, G. Savard, L. Chuang, and A. M. Rubin (2015), Magnitudes and moment-duration scaling of low-frequency earthquakes beneath southern Vancouver Island, *J. Geophys. Res. Solid Earth*, *120*, 6329–6350, doi:10.1002/2015JB012195.

Brune, J. N. (1970), Tectonic stress and the spectra of seismic shear waves from earthquakes, *J. Geophys. Res.*, *75*, 4997–5009.

Christensen, N. I. (1984), Pore pressure and oceanic crustal seismic structure, *Geophys. J. R. Astron. Soc.*, *79*, 411–423.

Ide, S., and G. C. Beroza (2001), Does apparent stress vary with earthquake size?, *Geophys. Res. Lett.*, *28*, 3349–3352, doi:10.1029/2001GL013106.

Gomberg, J., K. Creager, J. Sweet, J. Vidale, A. Ghosh, and A. Hotovec (2012), Earthquake spectra and near-source attenuation in the Cascadia subduction zone, *J. Geophys. Res.*, *117*, B05312, doi:10.1029/2011JB009055.

Hanks, T. C. (1982), f_{max}, *Bull. Seismol. Soc. Am.*, *72*, 1867–1879.

Hansen, R. T. J., M. G. Bostock, and N. I. Christensen (2012), Nature of the low velocity zone in Cascadia from receiver function waveform inversion, *Earth Planet. Sci. Lett.*, *337–338*, 25–38.

Harrington, R. M., and E. E. Brodsky (2009), Source duration scales with magnitude differently for earthquakes on the San Andreas Fault and on secondary faults in Parkfield, California, *Bull. Seismol. Soc. Am.*, *99*, 2323–2334.

Houston, H. (2015), Low friction and fault weakening revealed by rising sensitivity of tremor to tidal stress, *Nat. Geosci.*, *8*, 409–415, doi:10.1038/ngeo2419.

Houston, H., B. G. Delbridge, A. G. Wech, and K. C. Creager (2011), Rapid tremor reversals in Cascadia generated by a weakened plate interface, *Nat. Geosci.*, *4*, 404–409, doi:10.1038/ngeo1157.

Ide, S., G. C. Beroza, D. R. Shelly, and T. Uchide (2007), A scaling law for slow earthquakes, *Nature*, *447*, 76–79, doi:10.1038/nature05780.

Kennett, B. L. N. (1991), The removal of free surface interactions from three-component seismograms, *Geophys. J. Int.*, *104*, 153–154, doi:10.1111/j.1365-246X.1991.tb02501.x.

Ktenidou, O.-J., F. Cotton, N. A. Abrahamson, and J. G. Anderson (2014), Taxonomy of κ: A review of definitions and estimation approaches targeted to applications, *Seismol. Res. Lett.*, *85*, 135–146.

Madariaga, R. (1976), Dynamics of an expanding circular fault, *Bull. Seismol. Soc. Am.*, *66*, 639–666.

Matharu, G., M. G. Bostock, N. I. Christensen, and J. Tromp (2014), Crustal anisotropy in a subduction zone forearc: Northern Cascadia, *J. Geophys. Res. Solid Earth*, *119*, 7058–7078, doi:10.1002/2014JB011321.

Molnar, P., B. E. Tucker, and J. N. Brune (1973), Corner frequencies of P and S waves and models of earthquake sources, *Bull. Seismol. Soc. Am.*, *63*, 2091–2104.

Nicholson, T., M. G. Bostock, and J. F. Cassidy (2005), New constraints on subduction zone structure in northern Cascadia, *Geophys. J. Int.*, *161*, 849–859.

Nowack, R. L., and M. G. Bostock (2013), Scattered waves from low-frequency earthquakes and plate boundary structure in northern Cascadia, *Geophys. Res. Lett.*, *40*, 4238–4243, doi:10.1002/grl.50826.

Peacock, S. M., N. I. Christensen, M. G. Bostock, and P. Audet (2011), High pore pressures and porosity at 35 km depth in the Cascadia subduction zone, *Geology*, *39*, 471–474.

Park, J., C. R. Lindberg, and F. L. Vernon III (1987), Multitaper spectral analysis of high-frequency seismograms, *J. Geophys. Res.*, *92*(B12), 12,675–12,684, doi:10.1029/JB092iB12p12675.

Prieto, G. A., P. M. Shearer, F. L. Vernon, and D. Kilb (2004), Earthquake source scaling and self-similarity estimation from stacking P and S spectra, *J. Geophys. Res.*, *109*, B08310, doi:10.1029/2004JB003084.

Royer, A. A., A. M. Thomas, and M. G. Bostock (2015), Tidal modulation and triggering of low-frequency earthquakes in northern Cascadia, *J. Geophys. Res. Solid Earth*, *120*, 384–405, doi:10.1002/2014JB011430.

Rubinstein, J. L., J. E. Vidale, J. Gomberg, P. Bodin, K. C. Creager, and S. D. Malone (2007), Non-volcanic tremor driven by large transient shear stresses, *Nature*, *448*, 579–582, doi:10.1038/nature06017.

Rubinstein, J. L., M. L. Rocca, J. E. Vidale, K. C. Creager, and A. G. Wech (2008), Tidal modulation of nonvolcanic tremor, *Science*, *319*, 186–189, doi:10.1126/science.1150558.

Salisbury, M. H., and N. I. Christensen (1978), The seismic velocity structure of a traverse through the Bay of Islands ophiolite complex, Newfoundland, an exposure of oceanic crust and upper mantle, *J. Geophys. Res.*, *83*, 805–817.

Sato, T., and T. Hirasawa (1973), Body wave spectra from propagating shear cracks, *J. Phys. Earth*, *21*, 415–431.

Shelly, D. R., G. C. Beroza, S. Ide, and S. Nakamula (2007), Low frequency earthquakes in Shikoku, Japan, and their relationship to episodic tremor and slip, *Nature*, *442*, 188–191, doi:10.1038/nature04931.

Stachnik, J. C., G. A. Abers, and D. H. Christensen (2004), Seismic attenuation and mantle wedge temperatures in the Alaska subduction zone, *J. Geophys. Res.*, *109*, B10304, doi:10.1029/2004JB003018.

Tompkins, M. J., and N. I. Christensen (1999), Effects of pore pressure on compressional wave attenuation in young oceanic basalt, *Geophys. Res. Lett.*, *26*, 1321–1324.

Tompkins, M. J., and N. I. Christensen (2001), Ultrasonic P- and S-wave attenuation in oceanic basalt, *Geophys. J. Int.*, *145*, 172–186.

Yabe, S., A. S. Baltay, S. Ide, and G. C. Beroza (2014), Seismic-wave attenuation determined from tectonic tremor in multiple subduction zones, *Bull. Seismol. Soc. Am.*, *104*, 2043–2059.